In situ ^{10}Be modeling and terrain analysis constrain subglacial quarrying and abrasion rates at Sermeq Kujalleq (Jakobshavn Isbræ), Greenland

Brandon L. Graham[1], Jason P. Briner[1], Nicolás E. Young[2], Allie Balter-Kennedy[2], Michele Koppes[3], Joerg M. Schaefer[2], Kristin Poinar[1] and Elizabeth K. Thomas[1]

[1]Department of Geology, University at Buffalo, Buffalo NY USA
[2]Lamont-Doherty Earth Observatory, Columbia University, USA
[3]University of British Columbia, Vancouver, BC, Canada

Correspondence to: Jason P. Briner (jbriner@buffalo.edu)

Abstract. Glacial erosion creates diagnostic landscapes and vast amounts of sediment. Yet, knowledge about the rate by which glaciers erode and sculpt bedrock and the proportion of quarried (plucked) versus abraded material is limited. To address this, we quantify subglacial erosion rates and constrain the ratio of quarrying to abrasion during a recent, ~200-year-duration overriding of a bedrock surface fronting Sermeq Kujalleq (Jakobshavn Isbræ), Greenland, by combining ^{10}Be analyses, a digital terrain model, and field observations. Cosmogenic ^{10}Be measurements along a 1.2-m-tall quarried bedrock step reveal a triangular wedge of quarried rock. Using individual ^{10}Be measurements from abraded surfaces across the study area, we derive an average abrasion rate of 0.13±0.08 mm yr^{-1}. By applying this analysis across a ~1.33 km^2 study area, we estimate that the Greenland Ice Sheet quarried 378±45 m^3 and abraded 322±204 m^3 of material at this site. These values result in an average total erosion rate of 0.26±0.16 mm yr^{-1} with abrasion and quarrying contributing in roughly equal proportions within uncertainty. Additional cosmogenic ^{10}Be analysis and surface texture mapping indicate that many lee steps are relict from the prior glaciation and were not re-quarried during the recent overriding event. These new observations of glacier erosion in a recently exposed landscape provide one of the first direct measurements of quarrying rates and indicate that quarrying accounts for roughly half of total glacial erosion in representative continental shield lithologies.

1. Introduction

Distinctive features of glacier erosion characterize most glaciated regions, ranging from polished bedrock surfaces to overdeepened fjords. Additionally, vast amounts of sediment are produced via glacial erosion. The Greenland Ice Sheet accounts for a disproportionate delivery of sediment to the oceans, which impacts marine ecosystems and carbon sequestration (e.g., Overeem et al., 2017). The two dominant mechanisms of glacier erosion are subglacial quarrying and abrasion (Alley et al., 2019). Quarrying occurs when bedrock blocks are episodically entrained and removed by overriding glaciers (e.g., Hallet, 1996; Iverson, 2012, Koppes, 2022). Abrasion occurs via the gradual wearing down of bedrock surfaces as rock fragments are entrained and pressed into the bed by sliding ice (Hallet, 1979; Iverson, 1990, Koppes, 2022). The rate at which each of these processes occur is dictated by rock properties (e.g., Matthes, 1930; Dühnforth et al., 2010; Krabbendam and Glasser, 2011), glacio-hydraulic factors (e.g., Egholm et al., 2012; Zoet et al., 2013; Anderson, 2014) and climate (e.g., Cook et al., 2020; Koppes 2022). Although the result of the work done by glaciers on landscapes is dramatic, observational datasets that constrain how quickly landscapes are modified by ice remain sparse (Alley et al., 2019).

Despite considerable challenges in observing erosional processes occurring under ice, our understanding of subglacial erosion rates continues to expand. Total glacial erosion rates (i.e., abrasion + quarrying) have been inferred using a variety of both direct and indirect approaches (e.g., Hallet et al., 1996; Herman et al., 2021; Koppes, 2022) and are found to generally fall between 0.01 and ≥1 mm yr^{-1}; however, higher rates have been measured on short (annual to decadal) timescales (e.g., Koppes and Montgomery, 2009; Cowton et al., 2012). Attempts at separating the components of quarrying and abrasion have been made based on sediment flux measurements (e.g., Loso et al., 2004; Riihimaki et al., 2005), cosmogenic-nuclide inversions across subglacial bedforms (e.g., Briner and Swanson, 1998) and theoretical considerations related to sparsely vs. intensely fractured bedrock (e.g.,

Anderson, 2014). To date, measurements that isolate the eroded rock volume that can be attributed to quarrying are rare.

Here, we quantify subglacial erosion at a site that experienced a well constrained advance-retreat cycle of Sermeq Kujalleq (Jakobshavn Isbræ), a major outlet glacier in West Greenland (Fig. 1). We partition total erosion into abrasion and quarrying by pairing cosmogenic ^{10}Be measurements with analysis of a high-resolution terrain model and field mapping of bedrock surface textures. We model the accumulation of cosmogenic ^{10}Be that we measured across a quarried bedrock step to reconstruct the surface profile of the removed material, and the abrasion depth in adjacent surfaces. Our data allow us to identify which bedrock steps experienced quarrying during the most recent advance of the ice versus those unaltered since the prior glaciation. We thus calculate the volume of rock removed during the recent overriding event by abrasion and by quarrying, and estimate the average erosion rate of each over the duration of glacier overriding.

2. Study area

Greenland Ice Sheet margins are presently retreating, exposing terrain that was ice-covered during the latest Holocene advance that generally coincides with the Little Ice Age (Kjær et al., 2022). The north and south branches of Sermeq Kujalleq merged and extended westward ~35 km within the fjord to attain the "historical limit," which was observed in the fjord in 1850 CE (Fig. 1; Weidick and Bennike, 2007). Along the fjord, the historical limit is represented by a recognizable trimlines, and north and south of the fjord, prominent end moraines can be mapped to demarcate the extent of the "historical advance." In addition to the 1850 CE observation, this latest Holocene advance and retreat cycle has been dated in this region with lake sediment records (Briner et al., 2010, 2011) and a variety of imagery datasets (Csatho et al., 2007). The retreat of ice at our study site took place between 2008 and 2010.

During the Last Glacial Maximum, the Greenland Ice Sheet margin in the Sermeq Kujalleq sector rested on the continental shelf edge in Baffin Bay far west of Disk Bugt (e.g., Hogan et al., 2016). During the last deglaciation, the ice-sheet margin retreated eastward and eventually onto land on the eastern shores of Disko Bugt around 10,000 years ago. Later the ice margin retreated to within (east of) the extent of ice later attained during the historical limit. Prior authors calculated the timing of deglaciation to the historical limit at 7500 yr ago (Young et al., 2011; Balter-Kennedy et al., 2021) and to the present ice position by 7400 yr ago. It is thought that Sermeq Kujalleq receded during the Holocene deglaciation to a position ~20 km inland of the present ice margin (Weidick et al., 1990; Kajanto et al., 2020). We infer that ice flowed over our study site for a duration of 220±5 yr. The advance phase timing stems from prior research at an ice-dammed lake (which drained in 1990) that was first dammed (based on varve counts) around 1800 CE (Briner et al., 2011). As in Young et al. (2016), we estimate that the ice had advanced across our study area about a decade prior to it reaching the site of the ice-dammed lake, resulting in our estimate of 1790 CE as the timing of ice arrival at our study area. The retreat of ice from our study site in 2010 CE is based on historical imagery (Balter-Kennedy et al., 2021). Our study builds on Young et al. (2016) and Balter-Kennedy et al. (2021), who utilized cosmogenic ^{10}Be measurements to quantify total subglacial erosion rates of the gneissic bedrock in this area (Fig. 1).

3. Methods

In August 2018, we investigated a bedrock forefield adjacent to the north branch of Sermeq Kujalleq at 69.23°N and 49.81°W. The surface of glacially abraded and quarried bedrock exhibits pristine features of glacial erosion (Fig. 2). The study site contains competent, hard crystalline rock with widely spaced fractures (on the order of several meters). We measured ice-flow orientations, noted rock surface texture (variations in surface roughness are accompanied by tonal differences in the color of rock surfaces), used drone imagery to generate a high-resolution digital terrain model, and collected samples for cosmogenic ^{10}Be measurements.

Two stoss and lee landforms were chosen for detailed cosmogenic ^{10}Be analysis, with the goal of characterizing quarrying volume and timing. The premise of this approach requires no ^{10}Be in these surfaces inherited from prior to the previous glaciation, the LGM in this case. After extensive ^{10}Be dating in the region of heavily scoured surfaces, inheritance seems absent (e.g., Young et al., 2013). We chose one landform (Location A; Fig. 3A) to (1) estimate the dimensions of the bedrock removed based on the geometry of a quarried divot, where there is a sharp transition from rough to abraded surface roughness surrounding the quarried zone, and (2) use ^{10}Be concentrations in samples collected from the quarried divot to reconstruct the profile of the pre-quarried surface. We created a 3D forward model of cosmogenic ^{10}Be production to estimate the shape of the quarried material (single or multiple blocks) at location A. The fundamental set-up of our conceptual model is shown in Figure 4. At another site (Location B; Fig. 3B), there are two adjacent lee steps, each exhibiting a different surface roughness (one rougher, one smoother). Here, we measured the ^{10}Be concentration at the base of each step to test our hypothesis that different surface roughness relates to quarrying during the historical (Little Ice Age) overriding versus the prior LGM glaciation.

3.1 Field sampling for ^{10}Be analysis

At Location A, we measured ^{10}Be concentrations in five samples on the lee face: the top of the lee cliff ("surface"), from 12-15 cm, 30-33 cm, 65-69 cm and 110-115 cm at the base. Wide, thin samples were collected (30 cm W x 3-5 cm H x 2-4 cm D) to optimize the quartz mass within a narrow depth range and to minimize depth integration. We also collected three samples along the horizontal floor, two from within the quarried scar (1.2 and 2.1 m from cliff base) and one beyond the distal edge of the quarried scar from a polished surface (5 m from cliff base; Fig. 3). At Location B, we collected one sample from the base of the lee cliff from each zone (Fig. 3). All samples were collected with a combination of Hilti brand angle grinder with 5-inch diameter diamond bit blades, and hammer and chisel. At all sampling locations, field observations of topographic shielding were collected using a Brunton compass. Location and elevation were collected with a GPS time averaging smart phone application with ±5 m accuracy.

3.2 Terrain analysis and surface textures

Aerial imagery was collected with a DJI Mavic Pro unmanned aerial vehicle (UAV) with continuous and overlapping nadir imagery acquired using DJI smartphone app software. Maps Made Easy

(www.mapsmadeeasy.com; last access: April 26, 2023) was used to generate orthoimagery and a digital elevation model (DEM) of the field area using structure from motion principles (Graham, 2023). Mosaic imagery was used as a base layer for field mapping three surface roughness categories of the stoss and lee landforms based on the degree of freshness (1: freshly fractured exposed surfaces with minor grain-to-grain relief and no apparent abrasion, 2: lightly abraded, 3: heavily abraded and polished). We also observed that the fresh-appearing fracture surfaces exhibited darker surface colors, and that smoother surface textures exhibited lighter surface colors. The orientation of ice flow indicators consisting of striae, chatter marks and crescentic gouges were measured using a compass.

3.3 Beryllium-10 Laboratory Methods

All physical rock processing and isolation of quartz for ^{10}Be analysis was performed at the University at Buffalo Cosmogenic Isotope Laboratory (Corbett et al., 2016; Kohl & Nishiizumi, 1992). Pure quartz was processed at the Lamont-Doherty Earth Observatory cosmogenic dating laboratory following established beryllium extraction procedures. We processed eight samples from Location A, and two samples from Location B. AMS measurements of ^{10}Be/^{9}Be were performed at the Center for Accelerator Mass Spectrometry at Lawrence Livermore National Laboratory (LLNL-CAMS), with references relative to the 07KNSTD standard of known ^{10}Be/^{9}Be ratio of 2.85 x 10^{-12} (Nishiizumi et al., 2007). Measured 1σ analytical uncertainty ranged from 1.77% to 3.43% (Table 1). Apparent exposure ages were calculated using the online cosmogenic age calculator v3 (Balco et al., 2008) using the Baffin Bay ^{10}Be production rate calibration data set (Balco et al., 2008; Young et al., 2013). Apparent exposure age refers to the calculated age if the samples were at the surface and experienced zero erosion. Although these apparent ages are not used in our erosion models, they are instructive in analyzing and visualizing the context of the data based on a priori assumptions.

3.4 Cosmogenic Nuclide Modeling

Following Balco et al. (2011), we created a 3D forward model (Graham, 2023) of cosmogenic ^{10}Be production in the upper 1.2 meters of the glacially eroded bedrock at Location A using the known exposure and burial history. The history we adopt is shown in Fig. 4 and is as follows: Exposure from 7400 years ago to 1790 CE (~7200 years of exposure), burial from 1790 to 2010 CE (220 years of burial/erosion), and exposure from 2011 to 2018 CE (year of sample collection). We use the model to not only quantify the pre-quarrying surface, but also to determine the sensitivity of the specific sampling locations in the resulting divot. We thus prioritized certain sample locations from the vertical (lee) face to optimize the number of samples measured. To start, we simulated the ^{10}Be concentrations using a variety of pre-quarrying surface shape geometries ranging from a rectangular cross section to a triangular cross section to a geometry that is the same as the present-day surface. End members of these pre-quarrying surface options are illustrated as the purple, green and red lines in Figure 5B. Three-dimensional representations were generated by extending the 2D surface profiles laterally. This simplified the hypothetical surface models and was justified by the presence of laterally similar surface profiles observed on the landscape. Simulated cosmic particle bombardment was prescribed based on Gosse and Phillips (2001) for azimuth and elevation angles through the simulated overlaying bedrock to each sample location.

We next created an inverse model to solve for the pre-quarrying surface profile at Location A. An adaptive Metropolis Hastings Markov Chain Monte Carlo (MCMC) Matlab solver package (Haario et al., 2006) was implemented to estimate the parameters necessary to minimize the chi-squared reduction of the estimated ^{10}Be concentrations to the measured ^{10}Be concentrations. The unknown parameters were: 1) the surface profile x (horizontal distance within the quarried block) inflection point, 2) the surface profile z (depth) inflection point, 3) the depth of surface abrasion applied equally across all samples, and 4) the absolute attenuation length (Λabs) of the high energy neutron spallation through the rock. Acceptable a priori parameter ranges were initially prescribed (Table 1). We used the MCMC inversion to solve for the posterior parameters that correspond to the minimized ^{10}Be concentrations through the chi squared reduction. Due to the relatively shallow maximum sample depth (~1.2 meters) and small amount of abrasion previously estimated by Balter-Kennedy et al. (2021), muon production is minimal and approximately linear across the narrow depth range. Therefore, we treated production via muons as a linear function of depth across all sample sites, using a computationally efficient approximation of muon production rates near the earth surface (Balco, 2017).

The surface profile was generated via a point with X,Z coordinates located within the pre-quarrying geometries prescribed above. To expand laterally, a 25-point smoothed surface interpolation (Matlab function pchip) was applied between the generated point and the edges of the quarried block (top of the stoss cliff, and the rough-to-smooth transition around the perimeter of the quarried block). The initial estimate of abrasion depth for the model is based on an abrasion depth estimate from the surface sample 18JAK-Surface following the methods described in Briner and Swanson (1998) and Young et al. (2016) and is independent (but complementary) to results obtained by Balter-Kennedy et al. (2021). The absolute attenuation length (Λabs) is based on the range of values estimated in Gosse and Phillips (2001). Most estimations of spallation attenuation with depth rely on the apparent attenuation length (Λapp) because it assumes a horizontally infinite half space, or a flat surface profile, which the sample lays beneath at some depth, z (cm). Due to the off-zenith incoming cosmic particles travelling through an increasing length of mass, an integrated value of attenuation results in the apparent attenuation (Dunai, 2010). Because our research incorporates a complex surface model, the absolute attenuation length is required to properly simulate the attenuation through varying thicknesses of rock from off-zenith angles. Our inversion results in an estimate for an absolute attenuation length of 184±13 g cm^{-2}. When converted to an apparent attenuation length, via Λapp = (3.3/4.3)*Λabs, this becomes 141±10 g cm^{-2} and is within the range reported for the Arctic by Gosse and Phillips (2001).

3.5 Terrain analysis and volume of quarried material

We applied the resulting most probable profile of the quarried block at Location A (see Results) to other divots that were quarried during the historical advance. Incidentally, the shape of the quarried material is consistent with, and could largely be defined by, the non-quarried surfaces surrounding the quarried divots. Informed by results from the cosmogenic nuclide measurements at Location B and surface texture mapping, we identified which of the quarried divots were excavated during the historical advance versus glacier overriding associated with the last glaciation. The latter quarried zones were excluded from the analysis to prevent overestimating the quarried rock volume attributed

to the historical overriding event. All geographical information system (GIS) analysis was performed in QGIS Desktop 3.16 Long Term Release, with all datasets transformed to NSIDC Sea Ice Polar Stereographic North. The UAV-generated DEM, nominally 0.03 m raster cell size after transformation, was re-grided to 0.05 m cell size to which all further raster analysis was standardized. We defined our field area based on the extent of an exceptionally bedrock-rich part of the glacier forefield, with a higher degree of surface sediment cover around its periphery. Some areas of sediment cover from within our outlined study zone are excluded because they occluded accurate identification of the underlying surface texture and are not included in area calculations of the study site.

We defined the quarried zones attributed to the historical advance with polygons and removed them from the DEM of the present-day surface. We then interpolated a synthetic surface across the missing holes in the DEM to recreate the pre-1790 CE surface, or "paleo-surface" using the geometry guided by results from Location A. Next, we generated a difference map between the paleo-surface DEM and the present-day surface DEM. We then summed these values from the difference map. Finally, when applying the resultant abrasion rate across the study area, we estimated a cavity area below each of the historically quarried zones (assuming a seasonally averaged cavity roof of 45°) and subtracted this area from the total study area.

4. Results

The ^{10}Be concentrations from Location A (Table 2) decrease with depth and increase along the floor outwards from the lee cliff base (Fig. 5A & B). All samples result in lower apparent exposure ages than the estimated exposure duration of 7200 yr (7400 yr deglaciation minus 200 yr of subsequent burial), indicating that glacial erosion took place recently. The best fit of our forward model is a triangular wedge shape of removed material (Fig. 5B & C, green). This shape is supported by the surface morphology and textures adjacent to the quarried divot. Furthermore, this triangular wedge shape is supported by the MCMC model, which reveals a slightly concave pre-quarried block surface (see "MCMC" in Fig. 5B). Additionally, our MCMC modelling using all samples at Location A yielded a surface abrasion depth of 4.1±1.9 cm (Table 1). When using individual samples from the top (stoss) side of the lee ledge and from beyond the quarried divot, we derive abrasion depths of 2.7±1.1 and 5.8±1.1 cm, respectively.

To estimate an abraded volume of the study site, we consider several distinct abrasion rates calculated across the study area. Combining abrasion depths mentioned above with four nearby values reported by Balter-Kennedy et al. (2021) yields an average abrasion depth of 2.78±1.84 cm and an abrasion rate of 0.126±0.084 mm yr^{-1} (Table 3). Calculating the volume of material abraded requires the removal of areas where cavities existed in the immediate lee of bedrock steps. Although cavities change in size seasonally, we estimate that 12% of the field area consists of cavities assuming a 45° sloping cavity roof from the lip of bedrock steps. We thus calculate a volume of 323±204 m^3.

Results from Location B show significant differences in the measured ^{10}Be concentrations between the two lee steps. Sample ER2-A was collected at the base of an 85-cm-tall lee face that exhibits a fresh (non-polished) surface texture and a darker color (Fig. 3C). Its apparent exposure age of 2.3 ka (accounting for shielding using present topography) is significantly less than the expected age of ~7.2 ka, indicating quarrying during the historical

advance over the site. Sample ER2-B is from the base of a 120-cm-tall lee cliff and exhibits a lightly abraded texture and lighter color (Fig. 3B). Its apparent exposure age when accounting for shielding using present topography is 6.9 ka. We attribute the difference in apparent age of sample ER2-B and its expected age of 7.2 ka to a few centimeters of abrasion, and more importantly, to a lack of quarrying during the historical advance. Thus, the results from Location B indicate that other bedrock steps that exhibit smoother, lightly abraded surfaces were quarried during LGM glaciation, and that only rougher, darker-colored surfaces in some lee faces were quarried during the historical advance.

Our field mapping of rock surface textures exhibits quarried zones with a mixture of rough fractured and smooth abraded lee surfaces. We identified 73 quarried zones classified with rough-textured, dark-colored surfaces ("historical" quarrying) and 84 quarried zones classified as having slight smoothing and lighter surface tone (quarrying during the last glaciation; Fig. 6). Of the 73 quarried zones, 63 were identified as triangular shape based on the localized topography around each quarried zone, as was the case at Location A that we confirmed with cosmogenic nuclide measurements and modeling. The remaining 10 locations were identified as likely to have been rectangular blocks, and the rock volume quarried at these sites was calculated by doubling the volume generated by a triangular cross-section.

We calculate an area of quarried material during the historical advance of 1,635–2,050 m^2 (the derivation of this range is discussed below) of the total 13,256 m^2 field area (12–15%) and a quarried volume of 378±45 m^3 (Table 3). Using the duration of overriding during the historical advance, this equates to an equivalent quarrying rate of 0.13±0.03 mm yr^{-1} when averaged across the study site. We calculate a combined (total) eroded rock volume of 700±249 m^3 and total subglacial erosion rate of 0.26±0.16 mm yr^{-1}, of which 47% is attributed to abrasion and 53% is attributed to quarrying.

Measurements of ice flow indicators, including striations, crescentic gouges and chatter marks, reveal a south (180°) to southwest (225°) ice-flow direction (Fig. 7). When sorted by type of ice flow indicator, a pattern emerges showing an evolution of flow direction during the most recent ice advance. Small striations, being the most likely to represent the final ice-flow direction before deglaciation, show the most recent ice flow direction toward the south. Crescentic gouges and chatter marks, which are more likely to persist after some surface abrasion, reveal a southwesterly direction of ice flow. This shift likely represents the evolving flow direction and velocity change as ice flow over the field area increased in velocity, shifted to the southwest and thickened during the maximum phase of the historical advance. Although the velocity of ice over the study site during the maximum phase of the advance is not known, in 1985 when the site was still covered, surface velocity is in the 150-300 m yr^{-1} range (Howat, 2020). Based on the orientation of quarrying ledges and ice flow indicators, it appears that much of the quarrying occurred when the ice flowed southwest during what was presumably the highest ice flow velocity and thickness of the historical advance.

5. Discussion

We provide a new approach for quantifying the quarried volume of sediment across a glacial landscape and for establishing the relative contributions of quarrying and abrasion. Due to the inherent difficulty in measuring

quarrying directly, previous estimates rely on computational models or proxy inferences made from measurements of proglacial sediment discharge (Hallet, 1996; Loso et al., 2004; Riihimaki et al., 2005; Ugelvig et al., 2018). Quarrying estimates from stream sediments (e.g., bedload) require assumptions about the portion of the suspended load that is also derived from quarrying (Riihimaki et al., 2005). Here, our measurements of quarrying volume and rate stem from the combination of in situ ^{10}Be measurements and terrain analysis.

Our erosion rate measurements are similar to other estimates for glacial erosion in Greenland and beyond (Koppes and Montgomery, 2009; Cook et al., 2020). Our total erosion rate of 0.32±0.09 mm yr^{-1} is similar to what Balter-Kennedy et al. (2021) found at the same site using both surface ^{10}Be measurements (0.4–0.8 mm yr^{-1}) and a ^{10}Be depth profile from a 4-m-deep rock core (0.3–0.6 mm yr^{-1}). Although these rates are lower than those found using a sediment-budget approach in southwestern Greenland (4.8±2.6 mm yr^{-1}; Cowton et al., 2012), they are similar to centennial-scale erosion rate estimates of 0.29–0.34 mm yr^{-1} in northwestern Greenland (Hogan et al., 2020).

Quarrying is inferred to be highly dependent on glaciological and lithological conditions, including bedrock hardness and fracture spacing (Dühnforth et al., 2010; Krabbendam and Glasser, 2011; Iverson, 2012). Based on the hard nature of the bedrock with widely spaced fractures, we would expect abrasion to dominate at our field site (Dühnforth et al., 2010; Anderson, 2014). However, despite only 12–15% of the field site by area exhibiting recent quarrying, we calculate that 53% of total glacial erosion occurred as quarrying.

Our MCMC results and field observations suggest that, prior to quarrying, the bedrock surface was relatively low relief, likely with wave cavities in lee locations (Zoet et al., 2013) as opposed to stepped geometries that are more often considered in theoretical studies of quarrying (e.g., Anderson et al., 1982; Hallet, 1996; Iverson, 2012; Anderson, 2014). Despite bedrock characteristics inhibiting quarrying, the Greenland Ice Sheet experiences significant seasonal and sub-seasonal changes in subglacial hydrology in this area (Das et al., 2008; Andrews et al., 2014), which is thought to aid quarrying processes (Anderson, 2014; Ugelvig et al., 2018). Propagating fractures that are presumed to eventually lead to failure and quarrying appear to not solely rely on pre-existing fractures in the bedrock at our study site. The fracturing process, namely high clast-bed contact forces exerted by clasts embedded in basal ice pressing onto the bed, leads to the formation of crescentic gouges (Gilbert, 1906; Harris, 1943; Krabbendam et al., 2017) that we observed in abundance in the field (Fig. 2A). That many crescentic gouge trains increase in size toward quarried ledges–with a crescentic gouge at the lip of many edges–may indicate that gouge formation is a fracture nucleation point that leads to quarrying events in this field area (Figs. 2 and 8).

There are uncertainties associated with calculating erosion depth, volume and rate. We do not expect uniform abrasion across the study area given the stepped nature of the terrain and localized variations in basal stress. At Site A, we find a lower abrasion depth at the lip of the divot (2.7±1.1 cm) than the floor beyond the quarried zone (5.8±1.0 cm). We do not have enough data to elucidate predictable spatial patterns of more or less abrasion across the study site; instead, we rely on an average of a number of data points that provide a useful representative abrasion depth to apply across our field area.

It is useful to further consider uncertainties, such as those perhaps associated with our erosion thickness, volume and rate results. Abrasion depth estimates reported here have high uncertainty due to the inherent

measurement error in measuring cosmogenic nuclide concentration. An analysis of errors in Young et al. (2016) and Balter-Kennedy et al. (2021) for shallow abrasion depths shows a consistently appreciable uncertainty in relation to the low magnitudes of rock removal via abrasion. The measurement uncertainties for samples in the companion study of Balter-Kennedy et al. (2021) is ~2.5–3 cm, but when the estimated depth of abrasion is small and similar to mean uncertainty, the uncertainty can result in a significant range of the abraded depth. One advantage of our experiment at Location A is that multiple samples were used in the MCMC inversion, reducing the uncertainty in the estimated abrasion depth. Unfortunately, even with the added resolving power of multiple samples, the uncertainty in the abrasion depth is still 46%.

When converting the abrasion depth to an abrasion rate, another source of uncertainty is the duration of erosion. Whereas the timing of recent deglaciation and exposure is well constrained, the timing of burial is less well constrained. We use the overriding duration of 1790–2010 CE used in Balter-Kennedy et al. (2021), which is based on prior work in the area (Briner et al., 2011; Young et al., 2016). Although we use an absolute date range in our erosion rate calculations, the initiation of glaciation at the onset of the historical advance at our study site is reconstructed, not observed, and the initiation timing of overriding would affect the calculated erosion rates. If the ice arrived decades earlier (we think this is more likely than ice arriving later than 1800 CE), our calculated erosion rates would decrease, but the ratio of abrasion to quarrying, and the total depth of glacial erosion during the historical advance, would be unaffected.

An additional source of uncertainty relates to the reconstructed profile of the paleo-surface slope of quarried blocks, and thus of the volume of each removed block. We use the three-dimensional nuclide production inversion of the quarried zone at Location A to guide the shape for other quarried zones. To estimate the uncertainty of each quarried block, and the cumulative uncertainty of the quarried volume across the study site, each zone was analyzed for the likelihood of having a pre-quarrying sloped, triangular profile versus a more rectangular, stair-step profile. It is possible, perhaps likely, that at least some pre-quarried surfaces were somewhere between sloped (triangular block removed) and stepped (rectangular block removed), and not one or the other.

The uncertainty in our estimates of quarried rock volume is independent of the cosmogenic nuclide concentration. To estimate uncertainty in our manual outlining of each area of the quarried zones, a 0.5-meter buffer was extended at the edge of the floor of each quarried zone; this edge is based on changes in surface texture from rough to smooth as recorded in the high-resolution orthoimagery. The location of this transition is also dictated by the presence/absence of chatter marks/crescentic gouges, surface patina, and rock color. While many locations have a well-defined transition, 0.5 meters is an upper limit on our ability to define this boundary. The lee cliff is a well-defined feature on the landscape, and is accurately identified from the orthoimagery, with assistance using other products such as the DEM, and Hillshade/Roughness QGIS processing products. We consider our 0.5 m buffer on the extent along the quarried floor to be a conservative estimate. When used to define the volume of each block, we find that the 0.5 m buffer equates to a volume range of 379±45 m^3, and a quarried area of 1842±100 m^2 (12–15% of the study area).

Our inverse modeling of cosmogenic nuclide production at Location A highlights the continued importance of cosmogenic nuclides in glacier erosion studies. Optimizing sampling locations to estimate the parameters of

interest (surface geometry of a removed block, depth of abrasion, and attenuation length) was important for our inversion results. The sensitivity analysis to determine how samples were important in our forward model scenarios aided in sample selection for processing. The samples along the horizontal lee floor (FL1, FL2) are the most important for constraining the surface profile shape. Samples at the present-day surfaces (Surface, FL3) are the most important for constraining the depth of abrasion, while the samples collected along the vertical lee cliff are sensitive to the depth of abrasion and the attenuation length. In fact, not all samples collected along the vertical cliff were needed for the analysis, while additional samples along the floor near the quarrying-abrasion transition could have been beneficial.

6. Conclusion

Our pairing of cosmogenic nuclide analysis with inverse modeling of cosmogenic nuclide production through quarried material, along with topographic and morphologic analysis of a recently deglaciated bedrock landscape, provides one of the first direct observation-based estimates of glacial quarrying and partitioning of glacial erosion processes. We found that quarried volume generally matched that of abrasion despite a hard crystalline bedrock with wide fracture spacing and a low-relief surface morphology, all conspiring to limit quarrying. It seems that quarrying mostly took place via triangular wedge removal at this site. Field observations suggest clast-bed impacts evidenced by abundant crescentic gouges are a possible mechanism to nucleate quarrying events, assisted by seasonal and sub-seasonal fluctuations in subglacial water pressure. These results are a small addition to a field that needs further analysis. Yet, field data like these are important for grounding landscape evolution models with observational datasets and for providing fundamental information for understanding coupled glacier-hydrology-sediment production processes. Ultimately, the results of our work invite further analysis at this field site, including testing of both theoretical and computational models of glacial erosion.

Code and data availability

Code and data are available on GitHub at https://github.com/w0gpr/Cosmo3D (last access: April 26, 2023) and Zenodo (https://doi.org/10.5281/ZENODO.7858913; Graham, 2023).

Author contribution

BG, JPB, NEY and AB-K designed the study and collected field data. BLG, JPB and JMS led rock sample preparation and ^{10}Be analysis. BG modeled ^{10}Be production, computed terrain analysis, and derived erosion results. MK, KP and EKT provided significant input throughout the course of this research. BG and JPB prepared the paper with contributions from all co-authors.

Competing Interests

The contact author declares that none of the authors have any competing interests. Kristin Poinar is a member of the editorial board of The Cryosophere

Acknowledgements

We thank Chris Sbarra and Rosanne Schwartz for sample processing, CH2MHill Polar Field Services for supporting fieldwork, and Alan Hidy at Lawrence Livermore National Laboratory for beryllium isotope measurements. We also thank Maarten Krabbendam and Jakob Heyman for helpful reviewer comments.

Financial support

This research was supported by US National Science Foundation award #1504267 to Briner and #1503959 to Young and Schaefer.

References

Alley, R. B., Cuffey, K. M., and Zoet, L. K.: Glacial erosion: status and outlook, Ann. Glaciol., 60, 1–13, https://doi.org/10.1017/aog.2019.38, 2019.

Anderson, R. S.: Evolution of lumpy glacial landscapes, Geology, 42, 679–682, https://doi.org/10.1130/G35537.1, 2014.

Anderson, R. S., Hallet, B., Walder, J., and Aubry, B. F.: Observations in a cavity beneath Grinnell Glacier, Earth Surf. Process. Landforms, 7, 63–70, https://doi.org/10.1002/esp.3290070108, 1982.

Andrews, L. C., Catania, G. A., Hoffman, M. J., Gulley, J. D., Lüthi, M. P., Ryser, C., Hawley, R. L., and Neumann, T. A.: Direct observations of evolving subglacial drainage beneath the Greenland Ice Sheet, Nature, 514, 80–83, https://doi.org/10.1038/nature13796, 2014.

Balco, G.: Production rate calculations for cosmic-ray-muon-produced 10Be and 26Al benchmarked against geological calibration data, Quaternary Geochronology, 39,150-173, https://doi.org/10.1016/j.quageo.2017.02.001, 2017.

Balter-Kennedy, A., Young, N. E., Briner, J. P., Graham, B. L., and Schaefer, J. M.: Centennial- and Orbital-Scale Erosion Beneath the Greenland Ice Sheet Near Jakobshavn Isbræ, JGR Earth Surface, 126, https://doi.org/10.1029/2021JF006429, 2021.

Bernard, H.: A Theoretical Model of Glacial Abrasion, J. Glaciol., 23, 39–50, https://doi.org/10.3189/S0022143000029725, 1979.

Briner, J. P. and Swanson, T. W.: Using inherited cosmogenic 36Cl to constrain glacial erosion rates of the Cordilleran ice sheet, Geol, 26, 3, https://doi.org/10.1130/0091-7613(1998)026<0003:UICCTC>2.3.CO;2, 1998.

Briner, J. P., Young, N. E., Thomas, E. K., Stewart, H. A. M., Losee, S., and Truex, S.: Varve and radiocarbon dating support the rapid advance of Jakobshavn Isbræ during the Little Ice Age, Quaternary Science Reviews, 30, 2476–2486, https://doi.org/10.1016/j.quascirev.2011.05.017, 2011.

Cook, S. J., Swift, D. A., Kirkbride, M. P., Knight, P. G., and Waller, R. I.: The empirical basis for modelling glacial erosion rates, Nat Commun, 11, 759, https://doi.org/10.1038/s41467-020-14583-8, 2020.

Cowton, T., Nienow, P., Bartholomew, I., Sole, A., and Mair, D.: Rapid erosion beneath the Greenland ice sheet, Geology, 40, 343–346, https://doi.org/10.1130/G32687.1, 2012.

Das, S. B., Joughin, I., Behn, M. D., Howat, I. M., King, M. A., Lizarralde, D., and Bhatia, M. P.: Fracture Propagation to the Base of the Greenland Ice Sheet During Supraglacial Lake Drainage, Science, 320, 778–781, https://doi.org/10.1126/science.1153360, 2008.

Dühnforth, M., Anderson, R. S., Ward, D., and Stock, G. M.: Bedrock fracture control of glacial erosion processes and rates, Geology, 38, 423–426, https://doi.org/10.1130/G30576.1, 2010.

Dunai, T. J.: Cosmogenic Nuclides: Principles, Concepts and Applications in the Earth Surface Sciences, 1st ed., Cambridge University Press, https://doi.org/10.1017/CBO9780511804519, 2010.

Egholm, D. L., Pedersen, V. K., Knudsen, M. F., and Larsen, N. K.: Coupling the flow of ice, water, and sediment in a glacial landscape evolution model, Geomorphology, 141–142, 47–66, https://doi.org/10.1016/j.geomorph.2011.12.019, 2012.

Gilbert, G. K.: Crescentic gouges on glaciated surfaces, Geological Society of America Bulletin, 17, 303–316, https://doi.org/10.1130/GSAB-17-303, 1906.

Gosse, J. C. and Phillips, F. M.: Terrestrial in situ cosmogenic nuclides: theory and application, Quaternary Science Reviews, 20, 1475–1560, https://doi.org/10.1016/S0277-3791(00)00171-2, 2001.

Graham, B.: w0gpr/Cosmo3D: v1.0.0, https://doi.org/10.5281/ZENODO.7858913, 2023.

Haario, H., Laine, M., Mira, A., and Saksman, E.: DRAM: Efficient adaptive MCMC, Stat Comput, 16, 339–354, https://doi.org/10.1007/s11222-006-9438-0, 2006.

Hallet, B.: Glacial quarrying: a simple theoretical model, A. Glaciology., 22, 1–8, https://doi.org/10.1017/S0260305500015147, 1996.

Hallet, B., Hunter, L., and Bogen, J.: Rates of erosion and sediment evacuation by glaciers: A review of field data and their implications, Global and Planetary Change, 12, 213–235, https://doi.org/10.1016/0921-8181(95)00021-6, 1996.

Harris Jr, S.E.: Friction cracks and the direction of glacial movement, The Journal of Geology, 51, 244-258, https://doi.org/10.1086/625148, 1943.

Herman, F., De Doncker, F., Delaney, I., Prasicek, G., and Koppes, M.: The impact of glaciers on mountain erosion, Nat Rev Earth Environ, 2, 422–435, https://doi.org/10.1038/s43017-021-00165-9, 2021.

Hogan, K.A., Cofaigh, C.Ó., Jennings, A.E., Dowdeswell, J.A. and Hiemstra, J.F.: Deglaciation of a major palaeo-ice stream in Disko Trough, West Greenland, Quaternary Science Reviews, 147, 5-26, https://doi.org/10.1016/j.quascirev.2016.01.018, 2016.

Hogan, K. A., Jakobsson, M., Mayer, L., Reilly, B. T., Jennings, A. E., Stoner, J. S., Nielsen, T., Andresen, K. J., Nørmark, E., Heirman, K. A., Kamla, E., Jerram, K., Stranne, C., and Mix, A.: Glacial sedimentation, fluxes and erosion rates associated with ice retreat in Petermann Fjord and Nares Strait, north-west Greenland, The Cryosphere, 14, 261–286, https://doi.org/10.5194/tc-14-261-2020, 2020.

Howat, I.: MEaSUREs Greenland Ice Velocity: Selected Glacier Site Velocity Maps from Optical Images, Version 3 [Data Set]. Boulder, Colorado USA. NASA National Snow and Ice Data Center Distributed Active Archive Center. https://doi.org/10.5067/RRFY5IW94X5W. Date Accessed 07-26-2023, 2020.

Iverson, N. R.: Laboratory Simulations Of Glacial Abrasion: Comparison With Theory, J. Glaciol., 36, 304–314, https://doi.org/10.3189/002214390793701264, 1990.

Iverson, N. R.: A theory of glacial quarrying for landscape evolution models, Geology, 40, 679–682, https://doi.org/10.1130/G33079.1, 2012.

Joughin, I., Smith, B. E., Shean, D. E., and Floricioiu, D.: Brief Communication: Further summer speedup of Jakobshavn Isbræ, The Cryosphere, 8, 209–214, https://doi.org/10.5194/tc-8-209-2014, 2014.

Kajanto, K., Seroussi, H., de Fleurian, B., and Nisancioglu, K. H.: Present day Jakobshavn Isbræ (West Greenland) close to the Holocene minimum extent, Quaternary Science Reviews, 246, 106492, https://doi.org/10.1016/j.quascirev.2020.106492, 2020.

Kjær, K.H., Bjørk, A.A., Kjeldsen, K.K., Hansen, E.S., Andresen, C.S., Siggaard-Andersen, M.L., Khan, S.A., Søndergaard, A.S., Colgan, W., Schomacker, A. and Woodroffe, S.: Glacier response to the Little Ice Age during the Neoglacial cooling in Greenland, Earth-Science Reviews, 227, 103984, https://doi.org/10.1016/j.earscirev.2022.103984, 2022.

Koppes, M. N.: Rates and Processes of Glacial Erosion, in: Treatise on Geomorphology, Elsevier, 169–181, https://doi.org/10.1016/B978-0-12-818234-5.00032-8, 2022.

Koppes, M. N. and Montgomery, D. R.: The relative efficacy of fluvial and glacial erosion over modern to orogenic timescales, Nature Geosci, 2, 644–647, https://doi.org/10.1038/ngeo616, 2009.

Krabbendam, M. and Glasser, N. F.: Glacial erosion and bedrock properties in NW Scotland: Abrasion and plucking, hardness and joint spacing, Geomorphology, 130, 374–383, https://doi.org/10.1016/j.geomorph.2011.04.022, 2011.

Krabbendam, M., Bradwell, T., Everest, J.D. and Eyles, N.: Joint-bounded crescentic scars formed by subglacial clast-bed contact forces: Implications for bedrock failure beneath glaciers, Geomorphology, 290, 114-127, https://doi.org/10.1016/j.geomorph.2017.03.021, 2017.

Matthes, Francois E.: Geologic history of the Yosemite Valley, US Geological Survey, 1930. http://dx.doi.org/10.3133/pp160

Overeem, I., Hudson, B. D., Syvitski, J. P. M., Mikkelsen, A. B., Hasholt, B., van den Broeke, M. R., Noël, B. P. Y., and Morlighem, M.: Substantial export of suspended sediment to the global oceans from glacial erosion in Greenland, Nature Geosci, 10, 859–863, https://doi.org/10.1038/ngeo3046, 2017.

Riihimaki, C. A.: Sediment evacuation and glacial erosion rates at a small alpine glacier, J. Geophys. Res., 110, F03003, https://doi.org/10.1029/2004JF000189, 2005.

Ugelvig, S. V., Egholm, D. L., Anderson, R. S., and Iverson, N. R.: Glacial erosion driven by variations in meltwater drainage, J. Geophys. Res. Earth Surf., 123, 2863–2877, https://doi.org/10.1029/2018JF004680, 2018.

Weidick, A. and Bennike, O.: Quaternary glaciation history and glaciology of Jakobshavn Isbræ and the Disko Bugt region, West Greenland: a review, GEUS Bulletin, 14, 1–78, https://doi.org/10.34194/geusb.v14.4985, 2007.

Weidick, A., Oerter, H., Reeh, N., Thomsen, H. H., and Thorning, L.: The recession of the Inland Ice margin during the Holocene climatic optimum in the Jakobshavn Isfjord area of West Greenland, Global and Planetary Change, 2, 389–399, https://doi.org/10.1016/0921-8181(90)90010-A, 1990.

Young, N. E., Briner, J. P., Stewart, H. A. M., Axford, Y., Csatho, B., Rood, D. H., and Finkel, R. C.: Response of Jakobshavn Isbrae, Greenland, to Holocene climate change, Geology, 39, 131–134, https://doi.org/10.1130/G31399.1, 2011.

Young, N. E., Briner, J. P., Maurer, J., and Schaefer, J. M.: ^{10}Be measurements in bedrock constrain erosion beneath the Greenland Ice Sheet margin, Geophys. Res. Lett., 43, https://doi.org/10.1002/2016GL070258, 2016.

Zoet, L. K., Alley, R. B., Anandakrishnan, S., and Christianson, K.: Accelerated subglacial erosion in response to stick-slip motion, Geology, 41, 159–162, https://doi.org/10.1130/G33624.1, 2013.

Figure captions

Figure 1. A. Greenland. B. Study region August 2018; white line shows extent of Sermeq Kujalleq in 1850 CE and dashed line is 2018 terminus. C. Study area showing glacial erosion depths from Balter-Kennedy et al. (2021) and this study (star). D. Oblique drone photograph of the study area (point of view shown in C) showing study sites A and B (located near star in panel C).

Figure 2. Photographs of surfaces in the study area. A) Heavily abraded and polished surface showing one of the many "gouge trains", view to SW. B) Small lee step (approximately 20 cm high) within a heavily abraded and polished zone; note downflow from the lee cliff is a zone with more lightly abraded surfaces. C) Fresh surfaces with minor grain-to-grain relief and limited evidence for abrasion shown within quarrying "scars". D) Focus on a lee step (approximately 1 m high) showing the transition from a heavily abraded stoss surface (lightly colored) to darker-colored, fresh lee faces; some of the dark color in this image is from subglacial precipitate "staining".

Figure 3. A) Study location A; enclosed area is extent of the quarried material. Stars are locations of ^{10}Be measurements. B) Study location B; pair of quarried zones with a fresh, rough lee surface (left; sample ER2-A), and smooth, abraded lee surface (right, sample ER2-B).

564 **Figure 4.** Concept model for ^{10}Be production and concentration for the field area. 1) Retreat of the ice sheet from
565 the field area 7.4 ka. Erosion during the last glaciation is sufficient to remove ^{10}Be to background levels. 2) The
566 paleo-surface is exposed to cosmic radiation during the Holocene until ice overrides at ~1790 CE, building up ^{10}Be
567 in the upper ~2 m of bedrock. 3) Ice readvances and erodes via abrasion and quarrying during the historical
568 advance. 4) The present-day surface is exposed in 2010 CE.
569
570 **Figure 5.** A) Photograph of Location A (see also Fig. 3A) showing fresh quarried face and floor. B) Cross section
571 representation of the 3D model domain for Location A. Sample locations are marked as black boxes. The red line
572 shows the present-day surface profile, while purple and green lines show rectangular and triangular pre-quarrying
573 surface profiles, respectively, used in forward modelling. The thin gray lines are the minimized surface profiles from
574 the MCMC inversion. C) Measured (small circles) and simulated (lines in color) ^{10}Be concentration of the three
575 forward model scenarios; colors match top.
576
577 **Figure 6.** A. Orthoimage of the field area showing fractures (blue lines) and lee cliff faces (red lines). Zones
578 quarried during the most recent glacial advance are outlined in purple and sediment cover in yellow. Rose diagram
579 (inset) shows all measured ice flow indicators (in the direction of ice flow). B. Elevation difference in quarried
580 divots assigned to block removal during the historical advance.
581
582 **Figure 7.** The orientation of ice-flow indicators subdivided into type. Blue lines encompass orientations from all
583 ice-flow indicators combined (see Fig. 6).
584
585 **Figure 8.** Photographs showing the relationship between crescentic gouges and quarrying in the study area. A)
586 Gouge trains leading to a lee face with evidence for quarried flakes initiated by a gouge process (ice flow from
587 upper right to lower left). B) Example of angled (and polished) lee face from which a relatively thin flake has been
588 quarried and removed.
589

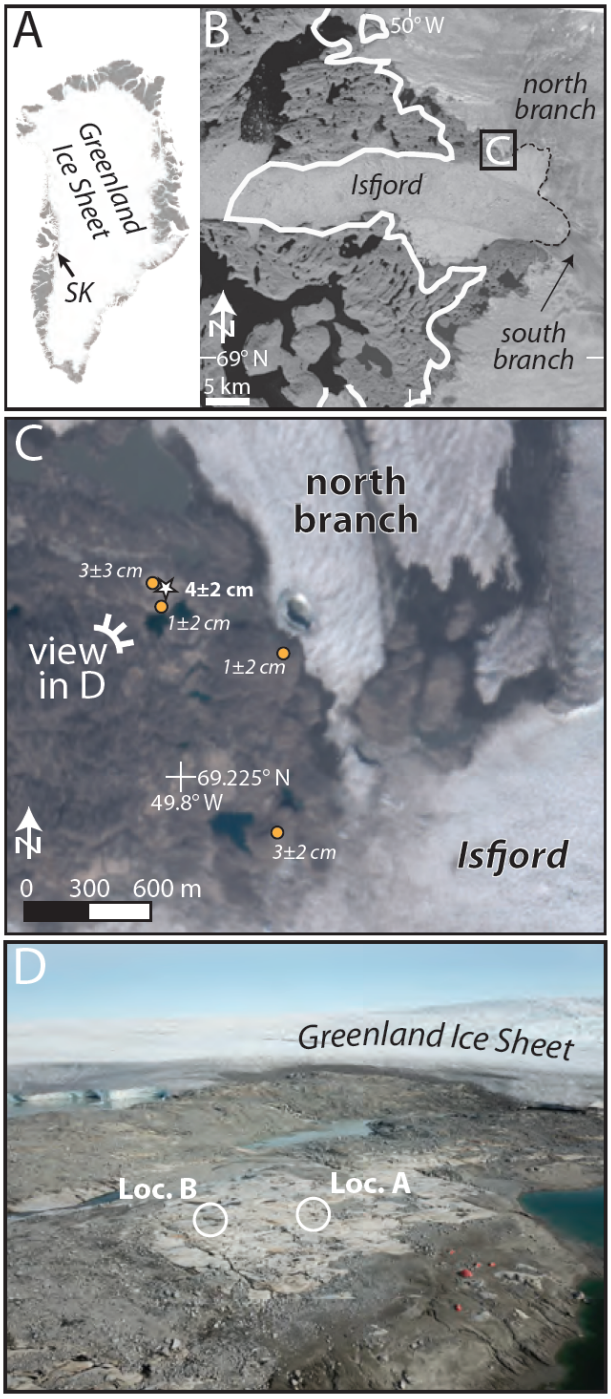

Figure 1. A. Greenland. B. Study region August 2018; white line shows extent of Sermeq Kujalleq in 1850 CE and dashed line is 2018 terminus. C. Study area showing glacial erosion depths from Balter-Kennedy et al. (2021) and this study (star). D. Oblique drone photograph of the study area (point of view shown in C) showing study sites A and B (located near star in panel C).

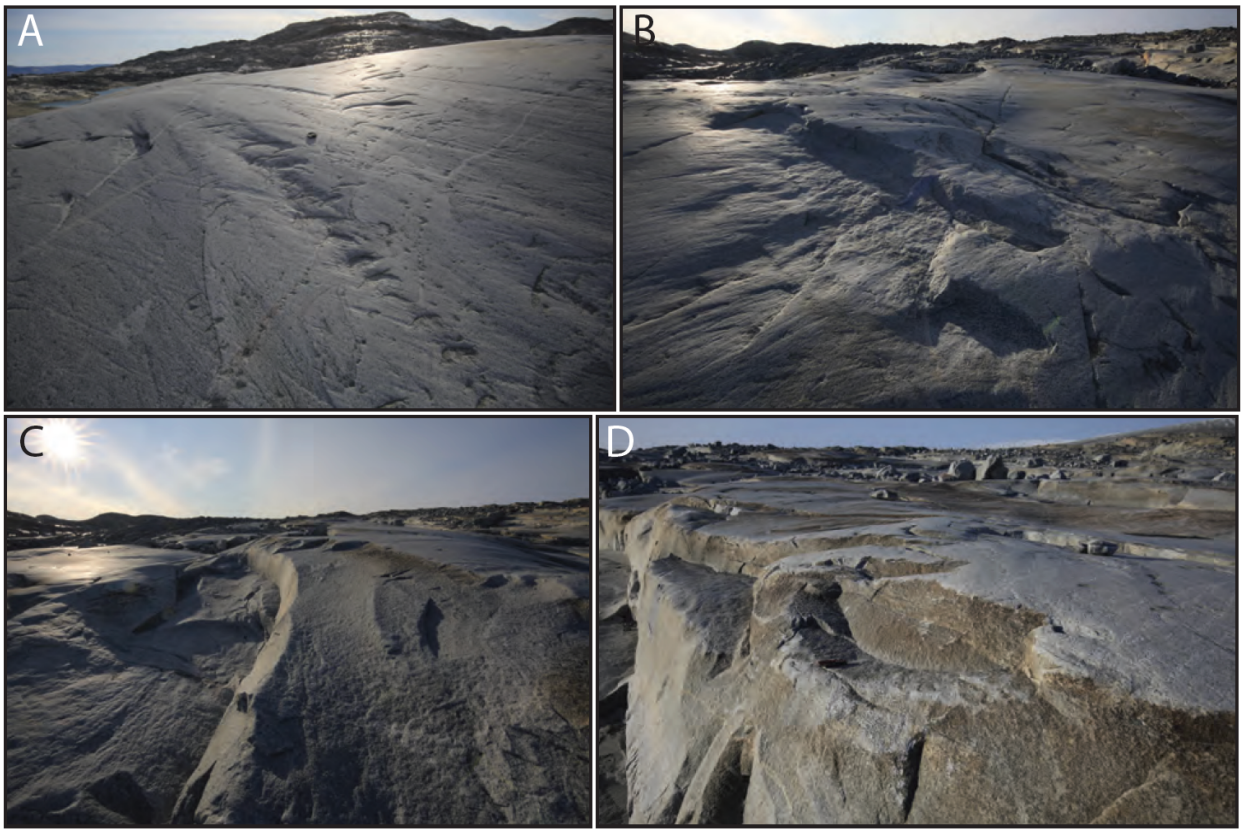

Figure 2. Photographs of surfaces in the study area. A) Heavily abraded and polished surface showing one of the many "gouge trains", view to SW. B) Small lee step (approximately 20 cm high) within a heavily abraded and polished zone; note downflow from the lee cliff is a zone with more lightly abraded surfaces. C) Fresh surfaces with minor grain-to-grain relief and limited evidence for abrasion shown within quarrying "scars". D) Focus on a lee step (approximately 1 m high) showing the transition from a heavily abraded stoss surface (lightly colored) to darker-colored, fresh lee faces; some of the dark color in this image is from subglacial precipitate "staining".

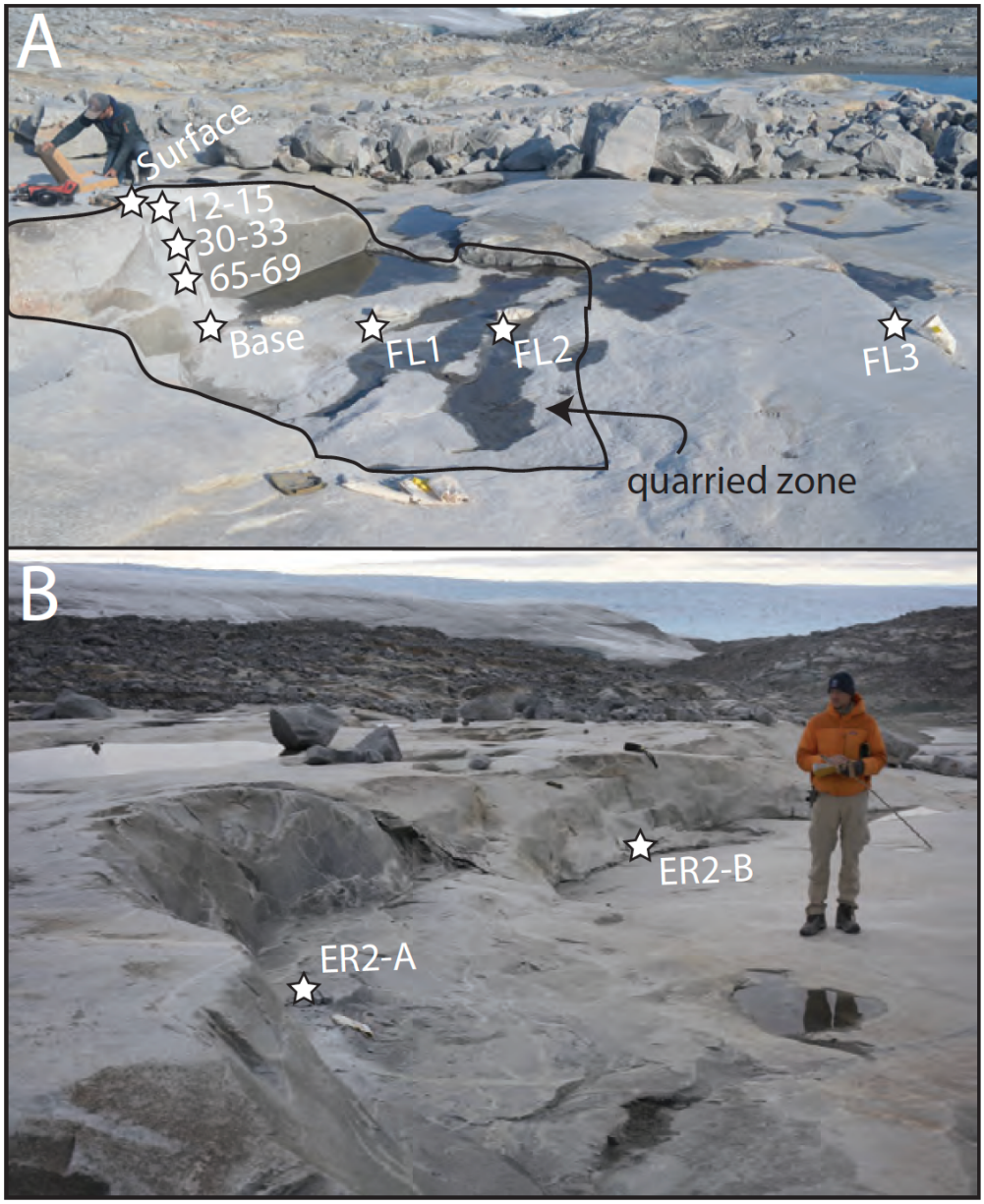

Figure 3. A) Study location A; enclosed area is extent of the quarried material. Stars are locations of ^{10}Be measurements. B) Study location B; pair of quarried zones with a fresh, rough lee surface (left; sample ER2-A), and smooth, abraded lee surface (right, sample ER2-B).

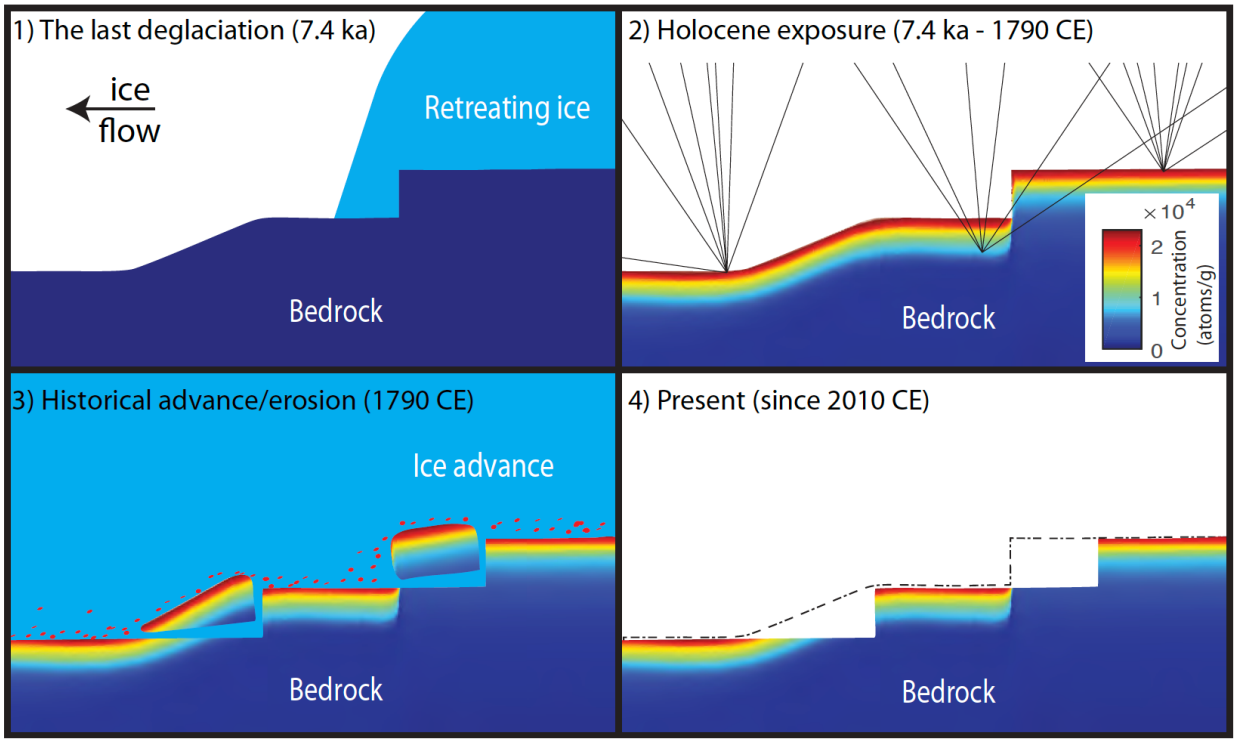

Figure 4. Concept model for ^{10}Be production and concentration for the field area. 1) Retreat of the ice sheet from the field area 7.4 ka. Erosion during the last glaciation is sufficient to remove ^{10}Be to background levels. 2) The paleo-surface is exposed to cosmic radiation during the Holocene until ice overrides at ~1790 CE, building up ^{10}Be in the upper ~2 m of bedrock. 3) Ice readvances and erodes via abrasion and quarrying during the historical advance. 4) The present-day surface is exposed in 2010 CE.

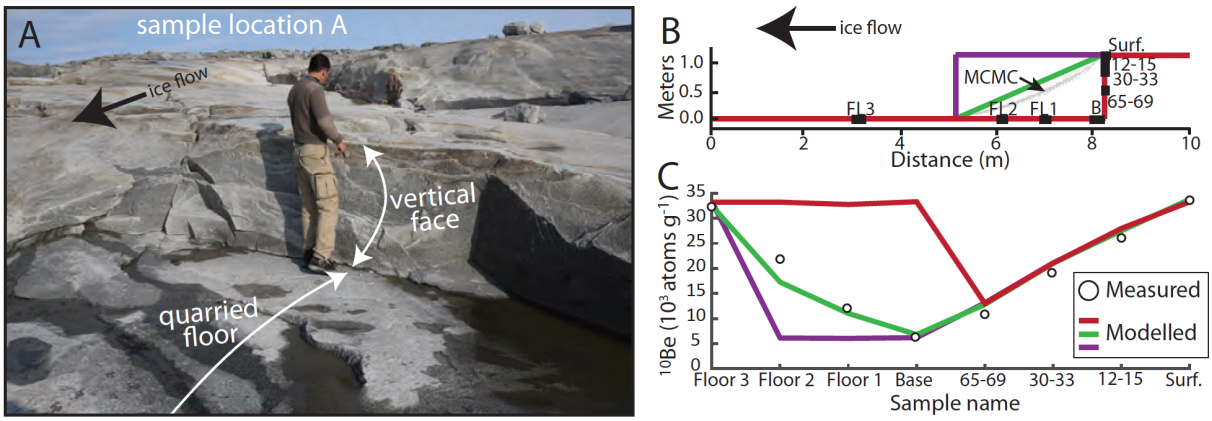

Figure 5. A) Photograph of Location A (see also Fig. 3A) showing fresh quarried face and floor. B) Cross section representation of the 3D model domain for Location A. Sample locations are marked as black boxes. The red line shows the present-day surface profile, while purple and green lines show rectangular and triangular pre-quarrying surface profiles, respectively, used in forward modelling. The thin gray lines are the minimized surface profiles from the MCMC inversion. C) Measured (small circles) and simulated (lines in color) ^{10}Be concentration of the three forward model scenarios; colors match top.

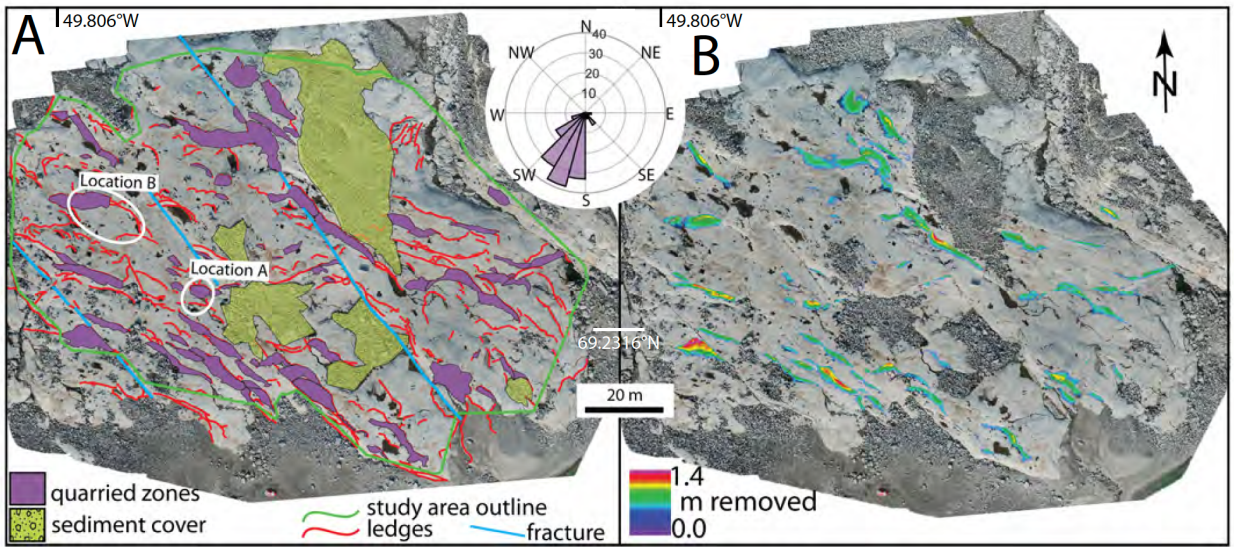

Figure 6. A. Orthoimage of the field area showing fractures (blue lines) and lee cliff faces (red lines). Zones quarried during the most recent glacial advance are outlined in purple and sediment cover in yellow. Rose diagram (inset) shows all measured ice flow indicators (in the direction of ice flow). B. Elevation difference in quarried divots assigned to block removal during the historical advance.

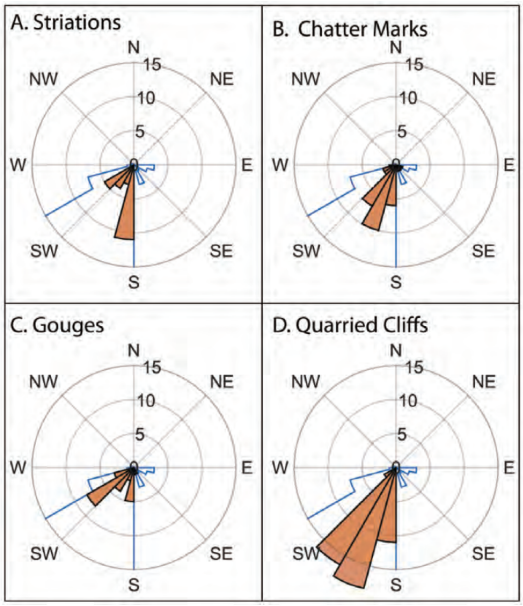

Figure 7. The orientation of ice-flow indicators subdivided into type. Blue lines encompass orientations from all ice-flow indicators combined (see Fig. 6).

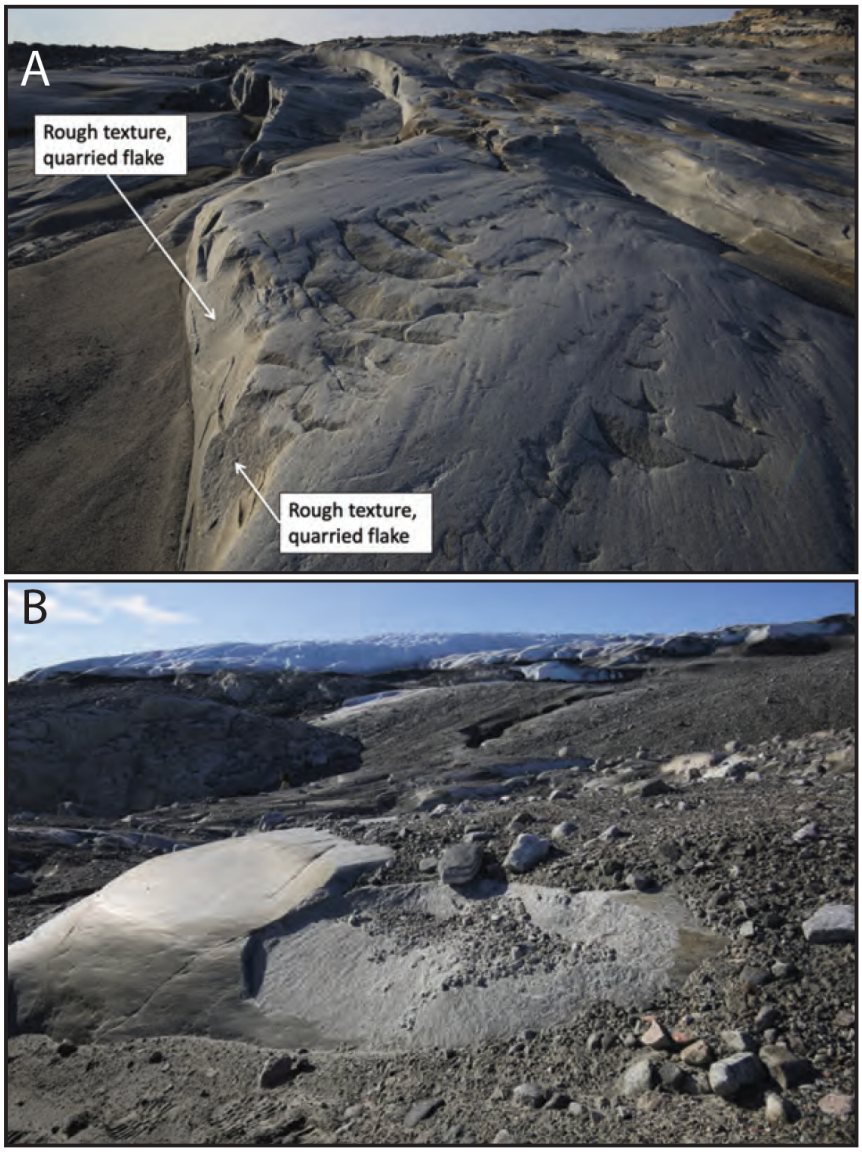

Figure 8. Photographs showing the relationship between crescentic gouges and quarrying in the study area. A) Gouge trains leading to a lee face with evidence for quarried flakes initiated by a gouge process (ice flow from upper right to lower left). B) Example of angled (and polished) lee face from which a relatively thin flake has been quarried and removed.

Table 1. MCMC parameters a prior and posterior.

	Initial	Input		Output	
Parameter Name	Guess	Minimum	Maximum	Mean	Std
xPoint	0.6	0	1	0.70353	0.18268
zPoint	0.6	0	1	0.50464	0.22515
Lambda (g cm^{-2})	208	150	240	184.26	12.518
Abrasion Depth (cm)	2.75	0	10	4.135	1.9038

The *a priori* input into the MCMC inverse and the posterior output from the model runs are those that minimized the chi squared reduction.

Table 2. Beryllium-10 sample data.

Sample Name	Sample thickness (cm)	Quartz Weight (g)	Carrier (g)	$^{10}Be/^{9}Be$ ($x10^{-14}$)	Blank Corrected ^{10}Be (atoms g^{-1})	Apparent Age (yr)
Surface	1.5	56.821	0.1817	15.3±0.3	33610±630	7100±130
12-15	3.0	55.872	0.1822	11.7±0.2	26090±490	5510±100
30-33	3.0	60.139	0.1830	9.2±0.2	19130±360	4030±80
65-69	4.0	64.043	0.1818	5.5±0.1	10730±240	2260±50
Base	5.0	34.677	0.1820	1.8±0.1	6210±210	1310±40
FL1	1.5	34.663	0.1832	3.3±0.1	11910±320	2510±70
FL2	1.5	45.816	0.1835	8.0±0.2	21870±500	4630±110
FL3	1.5	33.552	0.1832	8.5±0.2	31940±570	6740±120
ER2-A	5.0	26.190	0.1832	2.0±0.1	9150±310	1930±70
ER2-B	5.0	73.360	0.1834	14.6±0.3	25090±480	5300±100

Location A samples were located at 69.2316°N and 49.8093°W. Location B samples (ER2) at 69.2318°N and 49.8103°W. All samples were at an elevation of 107 meters above sea level. Sample density is 2.65 g cm^{-3}, and the 07KNSTD Be standard was used. The apparent age is the St scaling apparent exposure duration, assuming no shielding.

Table 3. Eroded rock volume and glacial erosion rates.

	Volume (m^3)	Area (m^2)	Rate (mm yr^{-1})
Abrasion	323±204	11,623*	0.13±0.08
Quarrying	378±45	1843±208	0.13±0.03
Total	700±249	13,256	0.26±0.16

*value is 12% less than total area because of estimated area of subglacial cavities